CrystEngComm

Cite this: *CrystEngComm*, 2012, **14**, 6957–6961

www.rsc.org/crystengcomm

PAPER

Morphology evolution of dendritic Fe wire array by electrodeposition, and photoelectrochemical properties of α-Fe_2O_3 dendritic wire array

Jin You Zheng, Myung Jong Kang, Guang Song, Se In Son, Sang Pil Suh, Chang Woo Kim and Young Soo Kang*

Received 2nd July 2012, Accepted 26th July 2012
DOI: 10.1039/c2ce26046h

In this paper, dendritic iron wire array films with different morphologies were prepared on Cu/ITO and slide ITO glass substrates by electrodeposition. The morphologies of Fe films obtained at different conditions were characterized by scanning electron microscopy. The growth mechanism of the dendritic Fe array is described by changing the ratio of deposition rate to mass transport rate (*R*) according to the experimental results. The variable *R* affects the final structure of the products. Especially, Fe dendrites can grow vertically layer by layer. The photoelectrochemical properties indicate that dendritic hematite (α-Fe_2O_3) arrays have a poor electron-hole (e–h) recombination effect.

1. Introduction

Electrodes modified by dendritic structured materials, which have high surface area since they consist of secondary, tertiary and even higher-order branches,[1–3] can be used as electrochemical and photoelectrochemical devices in many fields, such as fuel cells,[4–6] sensors,[1,5,7] batteries,[8,9] and catalysts.[10–14] The dendritic structure can be formed when the growth rate of crystals exceeds the mass transport rate of precursors that feed the growing crystals; in other words, the reaction forming the dendritic structure should be far from equilibrium. Electrodeposition offers great opportunity to adjust the material growth process away from equilibrium reaction so that the structure[15] and morphology[16] of nanomaterials can be tailored. The deposition rate in electrodeposition can be independently controlled by the deposition potential. Electrodeposition may also offer much freedom in altering the ratio of deposition rate to mass transport rate (*R*). Therefore, electrodeposition is an ideal method to synthesize dendritic structures.[2,17]

α-Fe_2O_3 photoelectrodes are of considerable importance in solar energy conversion materials due to their excellent properties, such as their small bandgap (2.1 eV), high resistance to corrosion and low cost.[18] Until now, uniform dendritic nanostructures of hematite were prepared directly by hydrothermal methods on the basis of weak dissociation of potassium ferricyanide ($K_3[Fe(CN)_6]$).[19–21] However, the product of these hydrothermal methods is a powder, not a film, which cannot be used as an electrode without further preparation. Recently Mohapatra and co-workers[22] have synthesized one-dimensional (1D) smooth α-Fe_2O_3 nanotubes on an Fe foil by the sonoelectrochemical anodization method. Mao and co-workers[23–25] have prepared highly ordered and vertically grown α-Fe_2O_3 nanorod or nanotube arrays by electrodeposition with anodic aluminium oxide (AAO) membrane templates followed by thermal calcination. However, for the anodization method, the electrolytic solution contains a noxious chemical NH_4F; for the AAO approach, the porous AAO should be prepared and a conductive layer on it is essential. Acid or alkaline treatment is necessary to dissolve the AAO after electrodeposition. In our recent work,[26] 1D dendritic Fe wire array film with ferromagnetism and superhydrophilic property could be directly prepared on a Cu substrate, and can be transformed into α-Fe_2O_3 without destroying the dendritic structure by thermal oxidation. However, the Cu substrate has some limitations for the application of dendritic α-Fe_2O_3 films in solar energy conversion or in water splitting fields. The Cu substrate is not optically transparent for absorbing solar light from the back side and it can also be easily oxidized by applied potential even when covered by a copper oxide (CuO and Cu_2O) film after annealing,[26,27] since $E^0_{Cu^{2+}/Cu}$ (*vs* SHE) is 0.34 V in the water splitting process. Therefore, the Cu substrate should be replaced with a transparent conductive oxide glass.

In our present study, the Cu/ITO[28] and bare ITO glass were used as substrates for electrodeposition of dendritic Fe films. The formation of various constructions of dendritic Fe films and the corresponding growth mechanism have been investigated. In addition, the dendritic Fe wire can be transformed into α-Fe_2O_3 without destroying the dendritic morphology by thermal oxidation. The photocurrent and photoresponse of the dendritic α-Fe_2O_3 films were measured to show the photoelectrochemical properties.

2. Experimental section

2.1 Preparation of Cu, Fe and α-Fe_2O_3 films

The deposition was carried out in a conventional three-electrode cell system using a PL-9 potentiostat. The commercial indium-doped tin oxide (ITO: 5 × 0.5 cm) (film thickness 200 nm,

Korea Center for Artificial Photosynthesis, Department of Chemistry, Sogang University, Seoul, 121-742, South Korea.
E-mail: yskang@sogang.ac.kr; Fax: (+82)-2-701-0967

resistance $\leqslant$ 10 Ω cm^{-2}) coated glass and Cu/ITO substrates were used as the working electrode. The substrate was dipped into the electrolyte solution vertically and the deposition area was 0.8 cm^2 or 0.5 cm^2. A coiled platinum wire and Ag/AgCl in 3 M KCl electrode were used as counter and reference electrodes, respectively. All potentials in this work measured *versus* Ag/AgCl electrode. All the electrodeposition experiments were carried out at room temperature (24 °C) without stirring or any external gas bubbling. The Cu/ITO substrate was obtained by electrodeposition from 5 mL aqueous solution containing 0.1 M $Cu(NO_3)_2 \cdot 2.5H_2O$ and 3 M lactic acid at pH 4 (by adding 4 M NaOH) at −0.4 V for 30 min.[28] Fe films were deposited on different substrates in 5 mL aqueous solution containing 0.05 M $FeSO_4$ and 0.1 M Na_2SO_4 at pH 2.5 (by adding 0.5 M H_2SO_4) at different applied potentials for a given time. α-Fe_2O_3 films were obtained by annealing Fe films under air at 500 °C for 3 h (heating speed 2 °C min^{-1}) in a furnace.

2.2 Characterization

The morphology of the material was characterized by scanning electron microscopy (SEM, Hitachi S-4300). Transmission electron microscopy (TEM, JEOL. JEM-2100F) with energy-dispersive spectroscopy (EDS, Oxford Instruments, INCA X-sight) was used to analyze the elemental composition of the obtained material. Photoelectrochemical measurements were conducted with a PL-9 potentiostat in a conventional three-electrode system in a V-style with a quartz window cell at room temperature under 1 sun (Asahi HAL-320, 100 mW cm^{-2}) illumination,[28] employing a Pt foil and an Ag/AgCl electrode as counter and reference electrode, respectively. Photocurrent potential was measured using linear sweep voltammetry (LSV) with a scan rate of 10 mV s^{-1} with a continuous light. 1 M NaOH was used as the electrolyte solution. Photoresponses were measured by chronoamperometry at constant potential of +0.6 V *vs.* Ag/AgCl.

3. Results and discussion

The Cu/ITO substrate obtained at pH 4 has a similar morphology to Cu/ITO at pH 5[28] as shown in Fig. 1a and b. The top-view and cross-sectional SEM images of dendritic Fe film, as shown in Fig. 1d and f, respectively, indicate that smooth triangular hierarchical structures were formed at the end of Fe dendritic wires, which blocks vertical growth of the wires. All the ends of wires are in the same plane and have triangular structure, and the length of the bottom wires (*ca.* 15 μm) is uniform. The formation of triangular ends, which have three primary branch arrays along three different directions with *ca.* 120° angles, is attributed to the natural construction of the dendritic wire,[26] since the dendritic fractals are generally formed under non-equilibrium conditions.[29,30] The reason that the ends stop the vertical growth and become smooth can be explained by the fact that the deposition rate becomes lower than the mass transport rate and the depletion zones disappear at the end of wires.[17] The density of Fe dendritic wires on Cu/ITO is lower than that on the Cu substrate probably caused by the different roughness of the substrate. Cu particles with some protruded tips can be formed into the initial depletion zones for the growth of the Fe dendritic structure; which is different with Fe dendritic wires grown directly on smooth polished Cu foil.[26]

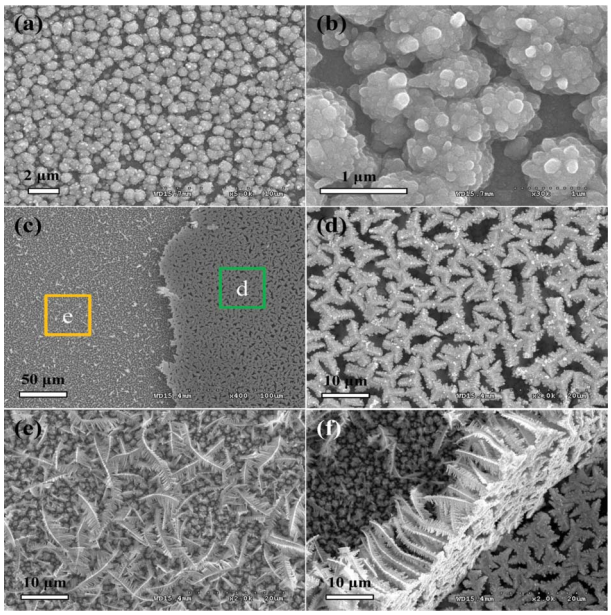

Fig. 1 (a) and (b) SEM images of Cu/ITO. (c) and (d) SEM images of dendritic Fe film deposited with −1.5 V for 10 min on Cu/ITO with deposition area of 0.5 cm^2. (d) and (e) Top views of the dendritic Fe film before and after scratching, respectively. (f) Cross-sectional SEM images of the dendritic Fe film.

Large areas of dendritic wires array with length of *ca.* 28 μm are formed on the surface of ITO as shown in typical SEM images in Fig. 2A-a and b. The aggregation of wires forms clusters, which have a similar structure to the Fe dendritic wire array on the Cu substrate; it is also caused by the capillary effect as we reported in our previous work.[26] The density of the wires electrodeposited on ITO is lower than that on the Cu substrate; therefore, the ravine-like gaps are very wide and a large amount of ITO glass is exposed without Fe dendritic wires covering. The different O element distribution mapping image compared with Fe as shown in Fig. 2A-c is attributed to the partial oxidation of Fe wire by air or remaining water. The atomic ratio of Fe to O is *ca.* 80 : 20 as shown Fig. 2A-d. This indicates that nanoscale Fe is very reactive to form oxides/hydroxides such as Fe_2O_3 or FeOOH. The color of the dendritic Fe wires film changed from black to brown in a short time after electrodeposition, as shown in the photograph of sample #1 in Fig. 2C. In some parts of dendritic Fe wire film (sample #2) obtained at the same deposition condition with sample #1, the effective mass transport rate is lower than the electrodeposition rate as the Fe^{2+} precursor consumes; the wires will stop the elongation of triangular unit[26] and form the smooth triangular ends since there is no concentration gradient around the tips of wires as shown in Fig. 2B-c, whereas the space hindrance effect (SHE) has no effect yet on the growth along the perpendicular direction. The ends can grow continuously under equilibrium conditions and all the ends can be connected to form one compact Fe layer (white color) on the top of dendritic wire array film as shown in Fig. 2B-d. Fig. 2B-a was checked from the marked area of sample #2 in Fig. 2C. We can easily observe from the rolled part that the uniform dendritic Fe wires array with large area was formed under the top layer film, as shown in Fig. 2B-b.

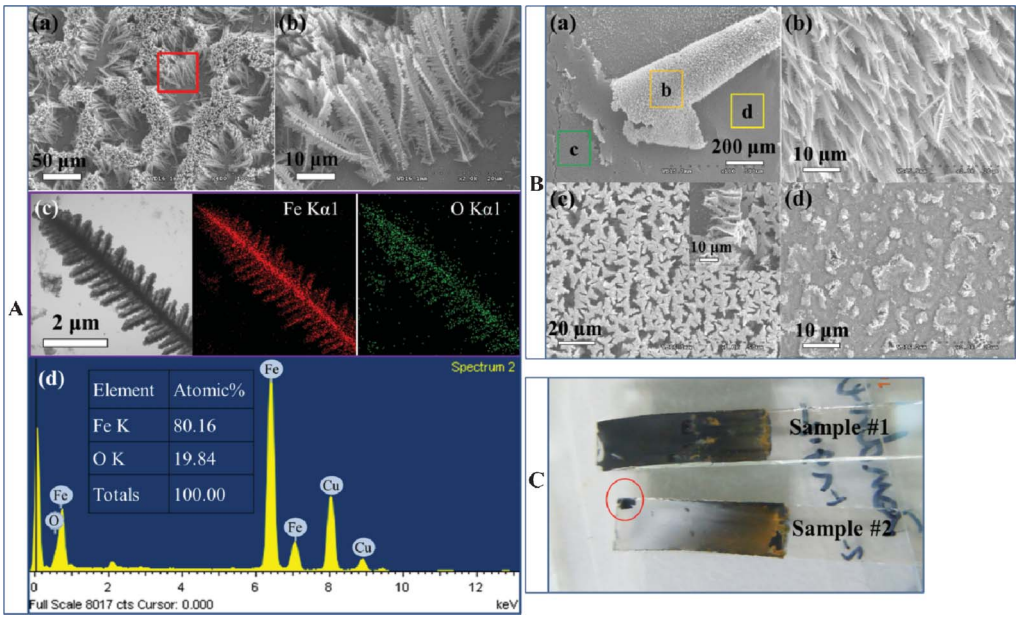

Fig. 2 A (sample #1): (a) and (b) SEM images, (c) EDS elemental mapping and (d) EDS spectrum of typical dendritic Fe wire array film. B (sample #2): (a) Low and (b)–(d) high magnification SEM images, corresponding to the marked area in (C). C: The photographs of sample #1 and #2. Sample #1 and #2 are obtained under the same conditions (−1.6 V for 10 min on ITO glass with deposition area of 0.8 cm^2) but have different morphologies.

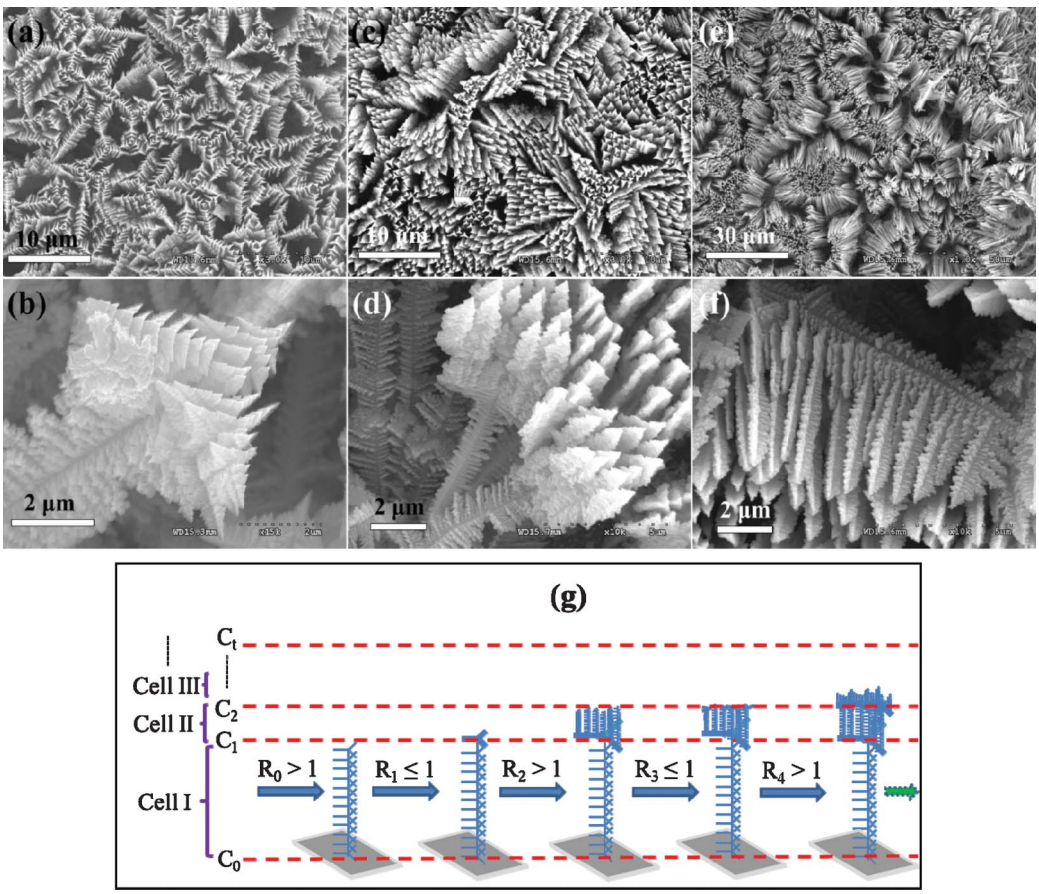

Fig. 3 (a)–(f) SEM images of Fe dendritic wire obtained at −1.5 V for 500 s on ITO glass with a deposition area of 0.5 cm^2. (g) Schematic representation of dendritic Fe wire growth at different stages with different *R* in the electrodeposition process. *R*: the ratio of deposition rate to the mass transport rate. *C*: the concentration of bulk solution at a certain distance with substrate.

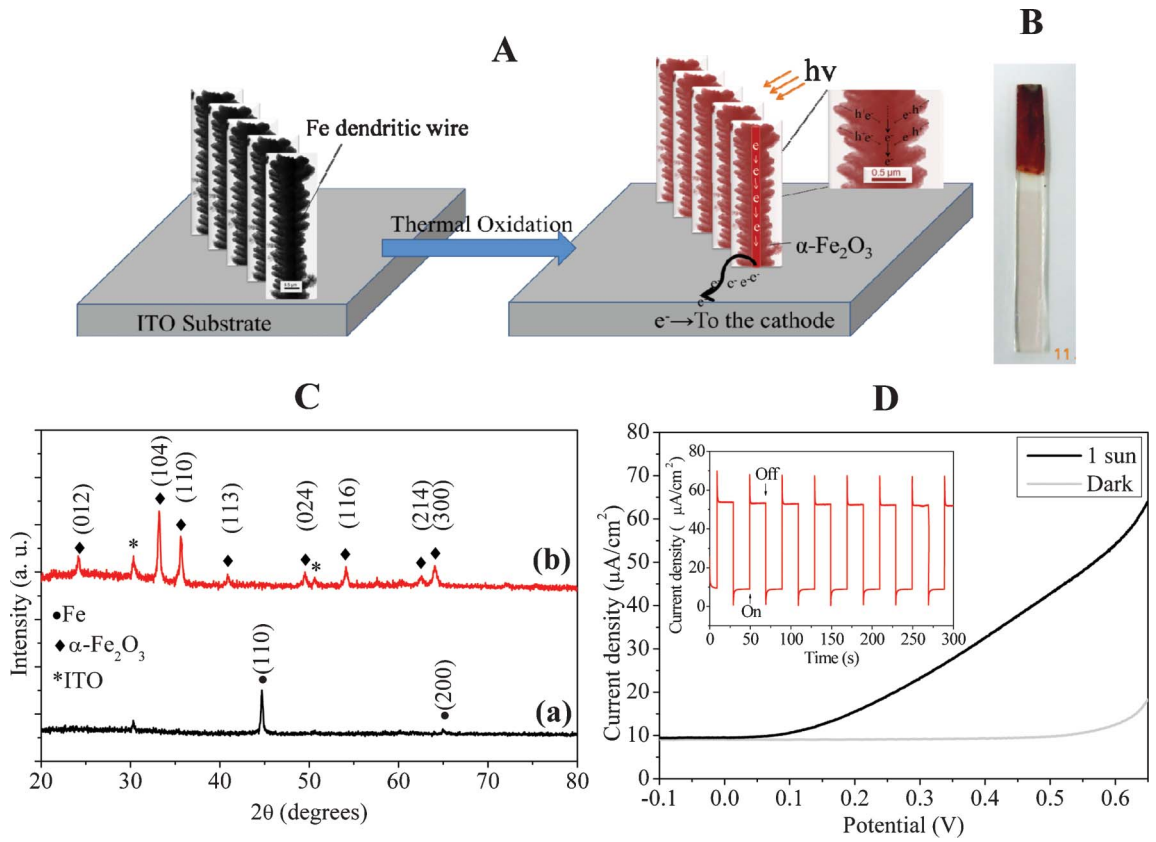

Fig. 4 (A) Schematic diagram showing the preparation process of dendritic Fe array film to dendritic α-Fe_2O_3 array film by a thermal oxidation method and the working process of dendritic α-Fe_2O_3 array anode. (B) A photograph of dendritic α-Fe_2O_3 film anode obtained by annealing dendritic Fe films (−1.6 V for 600 s on ITO glass with deposition area of 0.8 cm^2) under air at 500 °C for 2 h. (C) XRD patterns of (a) as-prepared and (b) post-annealing dendritic Fe films. (D) Current–potential characteristics of dendritic α-Fe_2O_3 films in 1 M NaOH under 1 sun illumination. Inset of (D) is the photoresponse at +0.6 V.

From the results obtained on the Cu/ITO and ITO slide, a similar phenomenon was observed that under non-equilibrium reaction the dendritic Fe wires can stop the growth along the perpendicular direction and start to grow along the parallel direction. In the deposition process, we found that the color of the dendritic Fe wires array (black color) will change to white if the wires stop growing; once the white color film with small area appears in the black film, it will spread quickly in several seconds as shown in the photograph of sample #1 and sample #2 in Fig. 2C. Therefore, the results should be due to the change of the ratio of deposition rate to the mass transport rate. The ends of dendritic wires can become smooth and stop the growth along the perpendicular direction as shown in Fig. 1d and Fig. 2B-c; in contrast, it can be supposed that the secondary dendritic wires can also grow on the ends of dendritic wires at some specific ratio of deposition rate to the mass transport rate ($R > 1$). Fig. 3a and b show that the ends of dendritic wires grow not only parallel but also perpendicularly. They show that the ends of secondary wires can also grow to form the triangular tower-like structures. Not only the ends of dendritic wires, but also the primary and secondary branches[26] of dendritic wires can grow continually as shown in Fig. 3e and f; for this case it should have concentration gradients around the branches of wires. All of the results can be the direct or indirect evidence to support the assumption as we mentioned.

A schematic representation of dendritic Fe wire growth conditions is given in Fig. 3g. In the initial growth process ($R_0 > 1$), the deposition rate is so fast that the Fe^{2+} precursor cannot supply sufficiently; the dendritic wires will grow with a similar growth mechanism as we reported in ref. 26. The length of wires becomes longer and longer as the deposition continues, and the neighboring dendrites will act as walls to block the mass transfer parallel to the substrate; thus the concentration of Fe^{2+} precursor in channels of the array will be so low so that it can be ignored. At some specific time ($R_1 \leqslant 1$), the deposition rate is equal or less than the mass transport rate because the precursor is being consumed; therefore, the vertical growth of ends can be stopped if the reaction is under equilibrium deposition. However, the ends will become smooth and the area will enlarge when the equilibrium deposition continues within some specific time interval; the smooth surface constructed by all smooth ends of wires will become a new "*substrate*" for deposition. These growth processes can occur several times in one single electrodeposition. As shown in Fig. 3c and d, this happened at least 2 times. To understand this phenomenon, it can be also assumed that the reactions were repeatedly happening at uninterrupted cells with different initial precursor concentration (C_t), such as the cell I with C_0 (0.05 M $FeSO_4$), cell II with C_1 and so on. It is possible to form special morphologies if such kind of phenomenon is happening in the electrodeposition of other materials.

The dendritic Fe array film can be easily transformed into α-Fe_2O_3 array film without destroying the dendritic structure by thermal oxidation as shown in the schematic diagram in Fig. 4A. The shape conservation during the transformation from Fe to α-Fe_2O_3 dendritic wires is quite different from the transformation from Co nanowires to CoO nanocrystallites.[31] The reason may be the slow heating rate (2 °C min^{-1}) and oxygen-rich annealing atmosphere in the former case, while the heating rate is much higher (50 °C min^{-1}) and annealing atmosphere is oxygen poor in the latter case. In addition, it required quite a high temperature (> 900 °C) for Co nanowires to fragment into CoO nanocrystallites. The annealed dendritic Fe array films obtained at −1.6 V for 600 s on ITO glass with deposition area of 0.8 cm^2 were investigated as one example to understand the basis of the photoelectrochemical properties of dendritic α-Fe_2O_3 array films. The length of Fe dendrite obtained at 600 s is about 30 μm. After thermal oxidation, the color of the Fe film changes from black to brownish-red as shown in Fig. 4B. Fig. 4C shows the XRD patterns of (a) as-prepared and (b) post-annealed dendritic Fe films. They can be perfectly indexed to Fe and α-Fe_2O_3 in terms of peak positions of JCPDS no. 65-4899 and 33-0664, respectively.[26] Fig. 4D shows the photocurrent and photoresponse of the dendritic α-Fe_2O_3 films in 1 M NaOH under 1 sun illumination; the onset potential is about 0.05 V *vs.* Ag/AgCl, which is lower than 0.2 V *vs.* Ag/AgCl for that of α-Fe_2O_3 nanorod arrays.[24] The reason that the onset potential shifted to negative direction is that the effective hole scavenging liberates more electrons making the anode potential more electronegative.[23] However, the onset potential of the dendritic α-Fe_2O_3 arrays is higher than that of α-Fe_2O_3 nanotube arrays.[22,23,32] As the potential scans to the positive direction, the anodic current increases gradually; the photocurrent can achieve around 43 μA cm^{-2} at +0.6 V. The photocurrent density here for dentritic α-Fe_2O_3 wires is 2 orders of magnitude lower than those reported for α-Fe_2O_3 nanowires and nanotubes.[23–25] Since hematite has several drawbacks such as a relatively low absorption coefficient, poor majority carrier conductivity and a short diffusion length (2–4 nm) of minority carriers,[33] a plausible explanation for such a low photocurrent is that the dendritic α-Fe_2O_3 wire is too long to achieve effective light absorption and extract the photogenerated electrons; another possible reason is that the dendritic arrays have a poor e–h recombination effect. The large initial anodic and cathodic spikes in the photoresponse curve could be evidence to show a higher electron-hole recombination effect for dendritic α-Fe_2O_3 array films. Further works need to be carried out for higher decreasing the electron-hole recombination.

4. Conclusions

In this work, morphology evolution of iron dendritic wire array films was studied by electrodeposition on Cu/ITO and ITO slide glass substrates. The final structures depended on the ratio of deposition rate to the mass transport rate, which was demonstrated by the construction of the dendritic wire ends. Fe dendrites can be grown layer by layer in the case of the variable ratio of deposition rate and the mass transport rate. The photocurrent of annealed Fe dendritic wire array film on ITO can reach about 43 μA cm^{-2} at +0.6 V *vs.* Ag/AgCl. The photoresponse curve indicates a poor electron-hole recombination effect for dendritic α-Fe_2O_3 array films.

Acknowledgements

This work was supported by the Korea Center for Artificial Photosynthesis (KCAP) located in Sogang University funded by the Ministry of Education, Science, and Technology (MEST) through the National Research Foundation of Korea (NRF-2009-C1AAA001-2009-0093879) and Collaborative Research Project under the NRF-NSFC Cooperative Program from National Research Foundation.

References

1 R. Qiu, X.L. Zhang, R. Qiao, Y. Li, Y. I. Kim and Y. S. Kang, *Chem. Mater.*, 2007, **19**, 4174.
2 K. S. Choi, *J. Phys. Chem. Lett.*, 2010, **1**, 2244.
3 P. K. Galenko and V. A. Zhuravlev, *Physics of Dendrites: Computational Experiments*, World Scientific, Singapore, 1994.
4 S. J. Ewing, R. Lan, X. X. Xu and S. W. Tao, *Fuel Cells*, 2010, **10**, 72.
5 R. Qiu, H. G. Cha, H. B. Noh, Y. B. Shim, X. L. Zhang, R. Qiao, D. Zhang, Y. I. Kim, U. Pal and Y. S. Kang, *J. Phys. Chem. C*, 2009, **113**, 15891.
6 K. Yamada, K. Miyazaki, S. Koji, Y. Okumura and M. Shibata, *J. Power Sources*, 2008, **180**, 181.
7 N. Zhang, K. Yu, Q. Li, Z. Q. Zhu and Q. Wan, *J. Appl. Phys.*, 2008, **103**, 104305.
8 Y. Hu, X. Huang, K. Wang, J. Liu, J. Jiang, R. Ding, X. Ji and X. Li, *J. Solid State Chem.*, 2010, **183**, 662.
9 H. Li, G. Zhu, X. Huang and L. Chen, *J. Mater. Chem.*, 2000, **10**, 693.
10 D. Chen and J. Ye, *Adv. Funct. Mater.*, 2008, **18**, 1922.
11 J. Huang, S. Vongehr, S. Tang, H. Lu and X. Meng, *J. Phys. Chem. C*, 2010, **114**, 15005.
12 J. Huang, S. Vongehr, S. Tang, H. Lu, J. Shen and X. Meng, *Langmuir*, 2009, **25**, 11890.
13 C. Gu, C. Cheng, H. Huang, T. Wong, N. Wang and T. Zhang, *Cryst. Growth Des.*, 2009, **9**, 3279.
14 Md. H. Rashid and T. K. Mandal, *J. Phys. Chem. C*, 2007, **111**, 16750.
15 X. H. Huang, L. Li, X. Luo, X. G. Zhu and G. H. Li, *J. Phys. Chem. C*, 2008, **112**, 1468.
16 X. H. Huang, G. H. Li, B. Q. Cao, M. Wang and C. Y. Hao, *J. Phys. Chem. C*, 2009, **113**, 4381.
17 C. M. Lopez and K.-S. Choi, *Langmuir*, 2006, **22**, 10625.
18 T. Ohmori, H. Takahashi, H. Mametsuka and E. Suzuki, *Phys. Chem. Chem. Phys.*, 2000, **2**, 3519.
19 M. Cao, T. Liu, S. Gao, G. Sun, X. Wu, C. Hu and Z. L. Wang, *Angew. Chem., Int. Ed.*, 2005, **44**, 4197.
20 S. Bharathi, D. Nataraj, M. Seetha, D. Mangalaraj, N. Ponpandian, Y. Masuda, K. Senthil and K. Yong, *CrystEngComm*, 2010, **12**, 373.
21 T. K. Van, H. G. Cha, C. K. Nguyen, S. W. Kim, M. H. Jung and Y. S. Kang, *Cryst. Growth Des.*, 2012, **12**, 862.
22 S. K. Mohapatra, S. E. John, S. Banerjee and M. Misra, *Chem. Mater.*, 2009, **21**, 3048–3055.
23 A. Mao, K. Shin, J. K. Kim, D. H. Wang, G. Y. Han and J. H. Park, *ACS Appl. Mater. Interfaces*, 2011, **3**, 1852–1858.
24 A. Mao, N. Park, G. Y. Han and J. H. Park, *Nanotechnology*, 2011, **22**, 175703.
25 A. Mao, G. Y. Han and J. H. Park, *J. Mater. Chem.*, 2010, **20**, 2247–2250.
26 R. Qiu, J. Y. Zheng, H. G. Cha, M. H. Jung, K. J. Lee and Y. S. Kang, *Nanoscale*, 2012, **4**, 1565.
27 L. S. Huang, S.G. Yang, T. Li, B. X. Gu, Y. W. Du, Y. N. Lu and S. Z. Shi, *J. Cryst. Growth*, 2004, **260**, 130.
28 J. Y. Zheng, G. Song, C. W. Kim and Y. S. Kang, *Electrochim. Acta*, 2012, **69**, 340.
29 T. A. Witten Jr. and L. M. Sander, *Phys. Rev. Lett.*, 1981, **47**, 351.
30 I. Lisiecki, P. A. Albouy and M. P. Pileni, *Adv. Mater.*, 2003, **15**, 712.
31 X. H. Huang, Z. Y. Zhan, X. Wang, Z. Zhang, G. Z. Xing, D. L. Guo, D. P. Leusink, L. X. Zheng and T. Wu, *Appl. Phys. Lett.*, 2010, **97**, 203112.
32 R. R. Rangaraju, K. S. Raja, A. Panday and M. Misra, *Electrochim. Acta*, 2010, **55**, 785–793.
33 K. Sivula, F. L. Formal and M. Gratzel, *ChemSusChem*, 2011, **4**, 432.